Three-dimensional Flow Field Characteristics of a Normal Slot Plasma Synthetic Jet Actuator

L. Cheng[1†], X. L. Sun[1] and S. Ma[2]

[1] *College of Aeronautical Engineering, Civil Aviation Flight University of China, Guanghan, 618307, China*
[2] *College of Flight Technology, Civil Aviation Flight University of China, Guanghan, 618307, China*

†Corresponding Author Email: chenglin2191343@cafuc.edu.cn

ABSTRACT

In this work, to comprehensively analyze the flow field characteristics of a normal slot plasma synthetic jet actuator, three-dimensional simulation models are established for both normal slot and normal orifice actuators. A detailed comparative analysis of the three-dimensional flow field characteristics of these two actuators is performed. The results indicate that the motion shockwaves and jets generated by the normal slot actuator cover a larger and more uniform region, showing planar characteristics and excellent flow control uniformity. The total pressure ratio for the normal slot actuator is 3.59, significantly higher than the value of 3.50 for the normal orifice actuator, indicating lower pressure loss in the former. Additionally, the normal slot has a larger average exit Mach number (Ma), indicating a stronger flow control capability. It also achieves the peak Ma in a shorter time, indicating a faster momentum output response. Therefore, compared with the normal orifice actuator, the normal slot actuator has better potential for flow control.

1. INTRODUCTION

When an aircraft deviates from its design point, it often experiences a deterioration in aerodynamic performance that can severely impact the normal operation of the aircraft. Flow control technology can effectively enhance the performance of an aircraft at off-design points. This flow control technology can be divided into two categories: active and passive flow control techniques (Falempin et al., 2015; Bayindirli, 2019; Bayindirli, 2023). Passive flow control offers the advantages of a reliable mechanical structure and stable control. However, it lacks the capability to adjust to operating conditions. Active flow control techniques achieve flow control by injecting mass, momentum, or heat. In addition, under varying conditions, active control techniques can adjust their methods and intensity of control, thereby providing better control efficacy. The adaptive regulation capability of active control techniques significantly surpasses that of passive control techniques, giving them a broader spectrum of applications. (Cattafesta, 2017).

Plasma flow control technology is an innovative approach that utilizes high-energy plasma fluids for active flow control. It has found widespread applications in flow separation control (Abdollahzadeh et al., 2018; Ebrahimi et al., 2018; Ebrahimi & Hajipour, 2018), airfoil lift enhancement (Meng et al., 2018), and shock wave control (Lapushkina et al., 2019; Liu et al., 2019). Plasma flow control technology achieves flow control through various means, such as jet momentum injection, thermal disturbances, and shock effects. In comparison to traditional active flow control technologies, plasma flow control technology offers advantages including a wide adjustable range, a quick response, and a high operating frequency, making it a focal point of recent domestic and international research on active fluid control technology.

Plasma flow control technology has been widely applied in the aerospace field, with three commonly used types of plasma aerodynamic actuators: local arc aerodynamic actuators (Falempin et al., 2015), dielectric barrier discharge actuators (Shaygani & Adamiak, 2023; Zhang et al., 2023), and plasma synthetic jet actuators (Zheng et al., 2023). The dielectric barrier discharge actuator has a lower flow velocity, making its application weaker under high-speed fluid control. The local arc aerodynamic actuator discharges directly into the mainstream, making the arc prone to interference, leading to unstable discharges. The plasma synthetic jet actuator studied in this paper was proposed and designed at Johns Hopkins University (Grossman et al., 2003). Compared with the other two forms of plasma actuators, the plasma

NOMENCLATURE			
T_a	amplitude of oscillation	E_s	total heating energy of the energy source term
p_a	cylinder diameter	t_A	heating time of the energy source term
HTC	Heat Transfer Coefficient	V	volume of the heating region
E_A	discharge energy	Q	power density of the energy source term
η	conversion efficiency of electrical energy into internal gas energy		

synthetic jet actuator has the advantages of a high jet velocity, stable and continuous internal discharge (Zong et al., 2018), and significant potential for application in high-speed flow control. Cybyk et al. (2004, 2005, 2006) established a model for the actuator's energy deposition stage and jet stage, identifying three stages in the working process: the energy deposition stage, jet stage, and suction recovery stage. Subsequently, Haack et al. (2010) improved the plasma synthetic jet analysis model and demonstrated good agreement in comparisons with experimental and simulation results.

The working process of the plasma synthetic jet actuator is characterized by high temperature, high pressure, drastic changes, and strong electromagnetic interference, which make it difficult to obtain initial information such as the temperature, pressure, and initial jet velocity. Therefore, numerical simulation studies on the pulse jet characteristics of a plasma synthetic jet actuator are needed (Zhang et al., 2020). Currently, numerical simulation methods for plasma synthetic jets mainly fall into two categories: one assumes that the arc heating time is short, treating the initial heating stage as an equivalent constant-volume heating process. Based on arc energy and energy efficiency calculations, the internal energy change of the gas can be obtained, and then the temperature and pressure parameters of the heated gas can be determined. These parameters are used as the initial conditions for the simulation (Haack et al., 2011). The second method involves adding an energy source term during the simulation to simulate the heating process. In terms of the energy, waveform, and time of discharge, the gas heating process is regarded as an energy source distributed in time and space. This method is more in line with a realistic gas heating process, resulting in higher accuracy in simulation results (Wang et al., 2013; Kim et al., 2019).

Current research on plasma synthetic jet actuators mainly focuses on the analysis of jet flow field characteristics (Emerick et al., 2014; Zhang et al., 2022a), the impact of electrical parameters (Belinger et al., 2011; Miao et al., 2021), and flow control applications (Luo et al., 2021; Zhang et al., 2022b; Zong & Kotsonis, 2019). It is noteworthy that the outlet form of plasma synthetic jet actuators commonly used by scholars is often a circular orifice. However, in practical jet flow control technology, a slot jet may contribute to improving the flow control uniformity and range. Additionally, most current simulation studies simplify the actuator into a two-dimensional model. This simplification results in a reduced ability to capture the three-dimensional characteristics of the actuator, especially the layout of the arc and outlet in the actuator, which significantly affects the flow field characteristics. Our team previously conducted experimental research on a normal slot plasma jet actuator (Cheng et al., 2017), demonstrating certain flow control advantages and unique flow field characteristics. However, due to measurement limitations, the experiment could only provide schlieren evolution images outside the actuator cavity, resulting in an insufficient understanding of the flow field and specific flow parameters inside the cavity. Considering these factors, in this work, we design a three-dimensional simulation model for normal slot and normal orifice actuators and conduct a detailed comparative analysis of the flow fields and parameter evolution of these actuators. The goal of this analysis is to explain the causes of the flow field characteristics observed in the experiment and to analyze the advantages of normal slot actuators in flow control.

2. COMPUTATIONAL METHOD

2.1 Mathematical Model and Numerical Method

The plasma jet process involves multiple disciplines, including plasma physics and fluid dynamics. The discharge process is extremely short and intense, reaching temperatures above 10,000 K. Therefore, establishing a comprehensive simulation model for plasma synthetic jets poses significant challenges. In this study, the method of adding an energy source term is employed to construct a simulation physics model, treating the discharge arc as a Joule heating source to rapidly heat the fluid inside the cavity. During the simulation, no ionization or chemical reactions are considered and it is assumed that the gas throughout the cavity is in a local thermodynamic equilibrium state.

The governing equations utilize the unsteady compressible viscous Navier–Stokes (N–S) equation set, with an energy source term added to the energy equation to simulate the heating process of the discharge arc. The solution of the governing equations is obtained using the commercial software Ansys® Fluent (2020 R2). The simulation employs an unsteady approach to solve the N–S equations, with the turbulence model set as the k-ε RNG model. In comparison to the standard k-ε model, the RNG model enhances the accuracy of simulating rapid strain flows. Additionally, the model incorporates the influence of vorticity on the turbulence, thereby improving the accuracy of the vorticity. Implicit differencing is used for discretization, and the spatial discretization utilizes a second-order upwind differencing scheme. The convective term discretization format is set as Roe-FDS. The heating process of the discharge arc in the studied plasma synthetic jet actuator mostly occurs within a few microseconds. Additionally, the flow parameters undergo rapid changes, representing a typical unsteady flow.
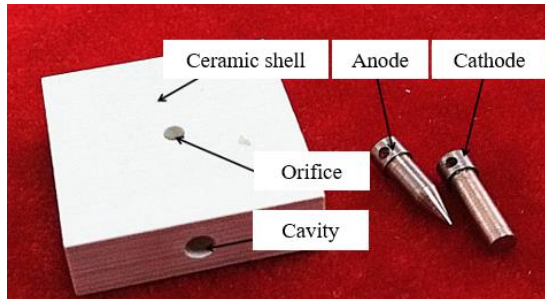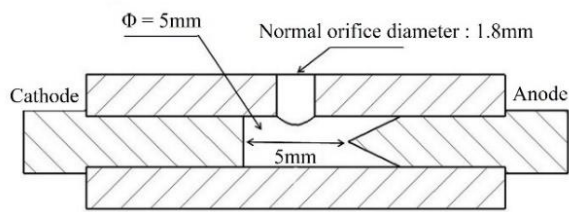
(a) The normal orifice actuator
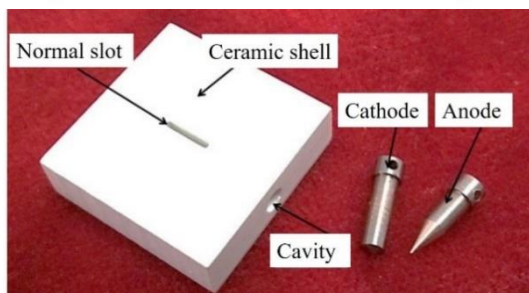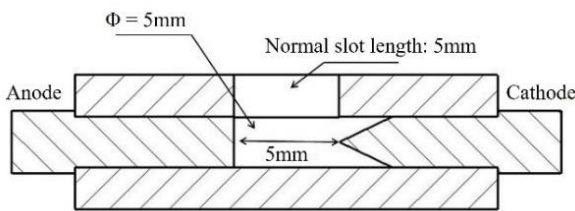
(b) The normal slot actuator
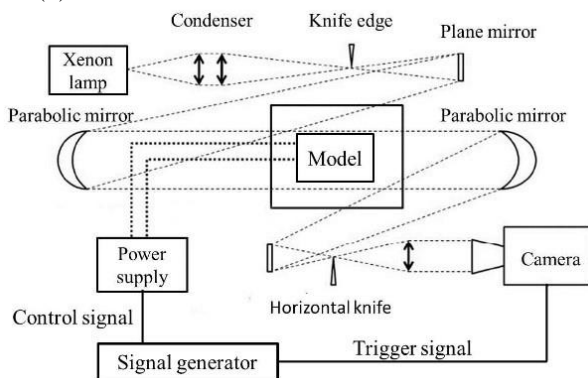
(c) Experimental setup

Fig. 1 A schematic diagram of the plasma synthetic jet actuators and experimental setup (Cheng et al., 2017)

Considering these factors, a time step of 3×10^{-9} s is selected for the simulation, with 25 iterations per time step. The convergence criteria for the simulation are defined as all variable residuals being less than 10^{-6}.

2.2 Geometrical Model and Computational Grid

In the experiment conducted by Cheng et al. (2017), two types of plasma synthetic jet actuators were designed.

A normal orifice actuator [Fig. 1(a)] served as the control for the normal slot actuator [Fig. 1(b)]. The external dimensions of the cavity were 15 mm × 15 mm × 6.4 mm, with 2.4 mm through-holes on the side for electrode installation. To ensure comparability between the experiments, the exit areas of the two cavity designs were kept the same. They were equipped with a vertical circular orifice with a diameter of 1.8 mm and a normal slot measuring 5 mm in length and 0.5 mm in width.

For the design of the geometric dimensions of the cavity, inspiration was primarily drawn from the work of Narayanaswamy et al. (2010). This small cavity actuator, designed for supersonic flow control, exhibits a substantial initial jet velocity, which enhances the momentum input capability. Furthermore, due to its compact size, the corresponding reduction in the operating cycle endows it with exceptional high-frequency operational characteristics.

The actuator was constructed using boron nitride ceramic and installed in the parallel optical path of the schlieren system. The schlieren system used a Z-shaped configuration. The experimental conditions included an ambient temperature of 287 K and a pressure of 101.67 kPa. The high-speed camera had an exposure time of 1 μs and a frame rate of 200,000 fps. The experiment effectively captured the internal flow beyond the jet exit. However, due to occlusion from the cavity, observation of the internal flow was limited. Consequently, the simulation domain was divided into two parts: the flow inside the cavity and the external flow.

A three-dimensional simulation model was constructed based on the above parameters to simulate the 3D model of the normal orifice actuator [Fig. 2(a)] and the 3D model of the normal slot actuator [Fig. 2(b)]. The simulation domain mainly consisted of four parts: the quiescent far field, jet outlet, cavity, and arc heating region. Considering the symmetry of the computational domain, only half of the flow field region was calculated to improve the computational efficiency. To avoid the influence of external boundaries on the evolution of the jet flow field, the dimensions of the external flow field were set to be 10 times the characteristic length of the outlet.

The computational grid for the flow field was generated using the Ansys® ICEM CFD (2020 R2) software, employing a structured mesh approach. Grid refinement was applied to critical flow regions such as the boundary layer, jet outlet, and arc heating zone. A grid growth rate of 1.05 was utilized, ensuring that the first layer grid in the boundary layer had a y^+ value less than 1. To assess grid independence, four different mesh configurations for simulating the normal slot actuator were designed, comprising 498,000, 996,000, 1,992,000, and 3,984,000 grid cells. The variation of the static pressure along the Y-axis on the jet axis is depicted in Fig. 3 for the four grid simulations.

The results reveal significant discrepancies in the case of 498,000 grid cells, with a reduction in this deviation observed for 996,000 grid cells. The simulations using 1,992,000 and 3,984,000 grid cells exhibit close agreement, indicating that the 1,992,000 grid cells yield
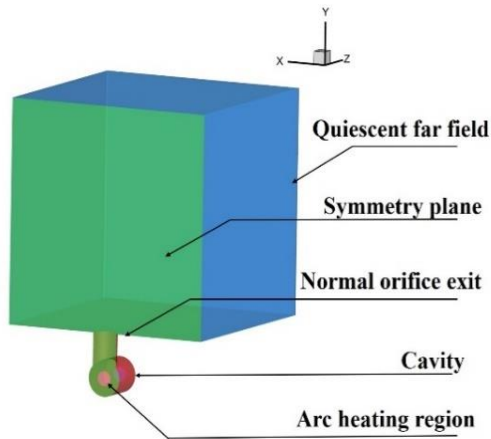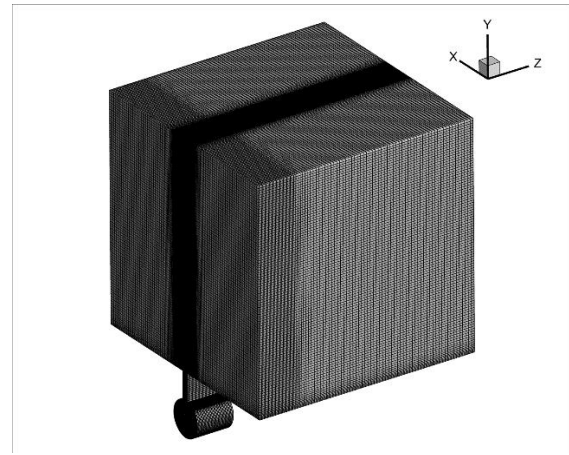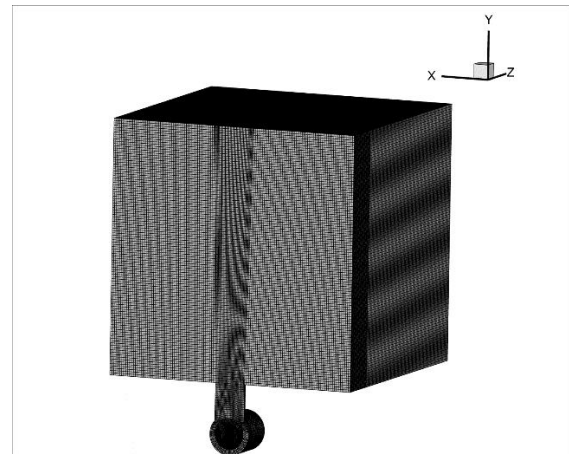
(a) The normal orifice actuator
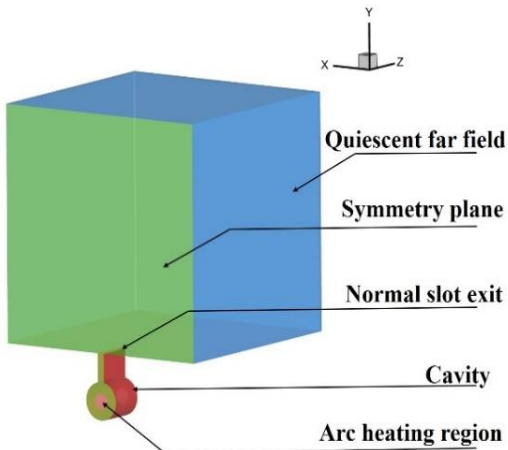
(b) The normal slot actuator

Fig. 2 A schematic of the 3D simulation model for plasma synthetic jet actuators

(a)   The normal slot actuator.

(b)   The normal orifice actuator.

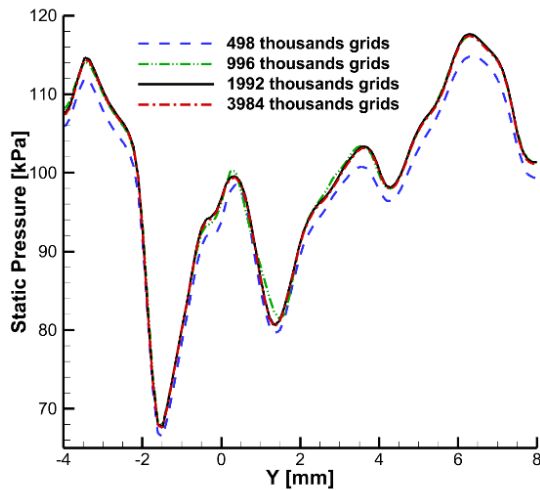**Fig. 4 A schematic of the computational mesh**

Fig. 3 The grid independence validation

sufficiently accurate simulation results. Considering the computational efficiency, this study adopts a mesh configuration with 1,992,000 grid cells for the simulations.

The simulation mesh for the normal slot actuator consisting of 1.992 million grid cells is illustrated in Fig. 4(a). The simulation mesh for the normal orifice actuator comprises 2.06 million grid cells and is depicted in Fig. 4(b).

2.3 Boundary Condition Settings

For the external flow field in the experiment, a pressure outlet boundary condition was applied. The boundary conditions were set based on the gas parameters reported in the study by Cheng et al. (2017), with a gas temperature (T_a) of 287 K and a pressure (p_a) of 101.67 kPa. The actuator cavity was treated as a solid wall, considering wall heat conduction, and a heat transfer coefficient (*HTC*) of 10 W/m²·K was specified.

According to the experimental electrical parameter measurements, the arc diameter was approximately 1 mm. Therefore, in the simulation, a cylindrical region at the center of the cavity with a diameter of 1 mm was designated as the arc heating region. Experimental measurements indicated discharge energies of 277 mJ and 218 mJ for the normal slot actuator and normal orifice actuator, respectively. This discrepancy in discharge energies is primarily attributed to inherent geometric differences between the two actuators during manufacturing, as even slight variations can lead to noticeable changes in electrical parameters.

To ensure comparability of the flow fields between the two actuators during the simulations, a discharge energy (E_A) of 218 mJ was selected for both. Additionally, drawing upon research by Belinger et al. (2011) on the

energy conversion efficiency, the conversion efficiency (η) of electrical energy to internal gas energy was taken to be approximately 25%. Consequently, the total heating energy from the energy source term (E_s) was calculated to be 54.5 mJ. Considering that the discharge energy is mainly injected within 9 μs, the heating time for the energy source term (t_A) was set to 9 μs.

The arc heating region was defined with a diameter of 1 mm and a length of 5 mm, resulting in a volume (V) of 3.93 mm³. Accordingly, the power density (Q) of the energy source term was calculated to be 1.54×10^{12} W/m³ using Eq. (1).

$$Q = \frac{\eta E_A}{V t_A} \tag{1}$$

2.4 Computational Method Validation

The simulation results for the normal slot actuator reveal that the jet reaches the outlet position 6 μs after heating initiation. Experimental data from Cheng et al. (2017) provided schlieren images at 10 μs intervals after the jet reached the outlet. Therefore, a comparison analysis was conducted between the experimental schlieren flow field at 10 μs after the plasma jet reached the outlet (Fig. 5) and the numerical schlieren image at 16 μs after heating initiation (Fig. 6). Figure 5 shows the schlieren image of the plasma jet 10 μs after emerging from the outlet. It is observed that the normal slot plasma jet is primarily composed of precursor shock waves, reflected waves, and high-temperature jets. Additionally noteworthy is the extended straight section of the shock wave in the slot-width direction, which exhibits characteristics of planar shock waves. Figure 6 shows the numerical shadowgraph image at this moment, demonstrating the excellent simulation of the flow field structure by the computational method. The simulation accurately captures the main flow field features, including precursor shock waves, reflected waves, and high-temperature jets.

To quantitatively assess the reliability of the computational method, measurements were taken of the jet front position in the simulation results at intervals of 10 μs after the jet reached the outlet. Figure 7 shows a

(a) Length direction   (b) Width direction

Fig. 6 Numerical schlieren images 16 μs after the initiation of arc heating for the straight slot actuator (1 - precursor shock wave, 2 - reflected wave, 3 - jet front)
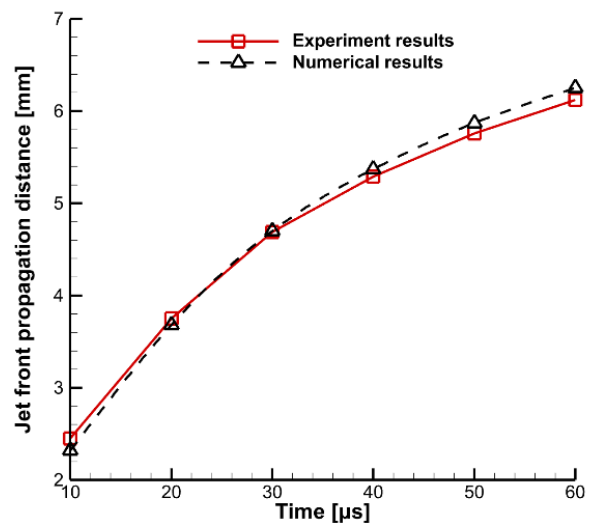
Fig. 7 Plasma jet front position: experimental and simulated results

comparison between the simulated measurements of the jet front position and the experimental data. Discrepancies between the simulation and experimental results are observed before 20 μs and after 30 μs. These differences mainly stem from inaccuracies in estimating the energy efficiency and the simulation's inability to capture vortex dissipation at small scales. Overall, the simulation method effectively replicates the temporal variation pattern of the jet front position with reasonable accuracy, indicating that the simulation approach is highly credible.

3. RESULTS AND DISCUSSIONS

Cheng et al. (2017) conducted a comparative experimental study on normal slot and normal orifice plasma synthetic jet actuators. Their experiment provided high-speed schlieren images of the flow evolution from both the normal slot and normal orifice actuators, as depicted in Fig. 8. The experiment revealed that, with an equal outlet area, the initial jet velocity of the plasma synthetic jet from the normal slot actuator was faster than that from the orifice actuator. Within the three-dimensional flow field structure of the normal slot plasma synthetic jet actuator, superior planarity was observed in
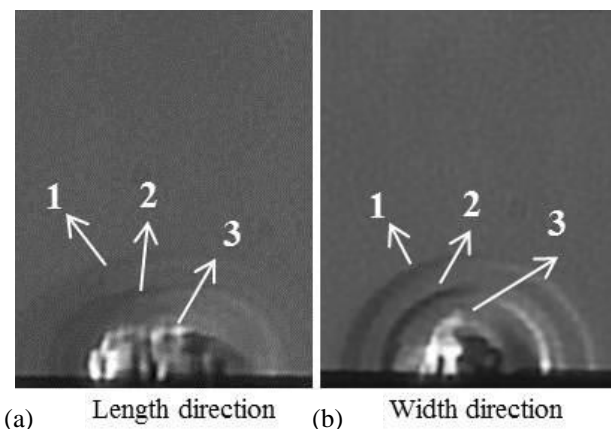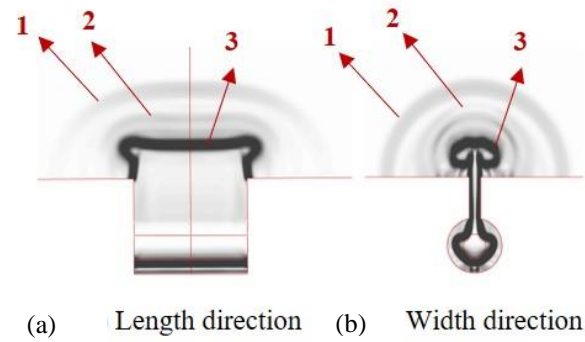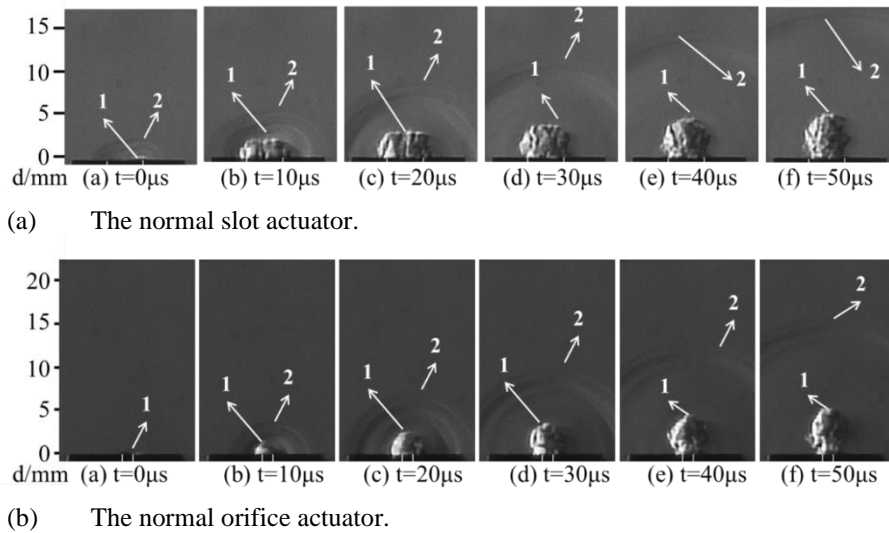

(a) Length direction   (b) Width direction

Fig. 5 Experimental schlieren images 10 μs after the emission from the outlet of the normal slot actuator (1 - precursor shock wave, 2 - reflected wave, 3 - jet front) (Cheng et al., 2017)

(a)　　　The normal slot actuator.

(b)　　　The normal orifice actuator.

Fig. 8 Time delayed schlieren images of the normal slot actuator and orifice actuator (1- jet front，2- precursor shock wave)
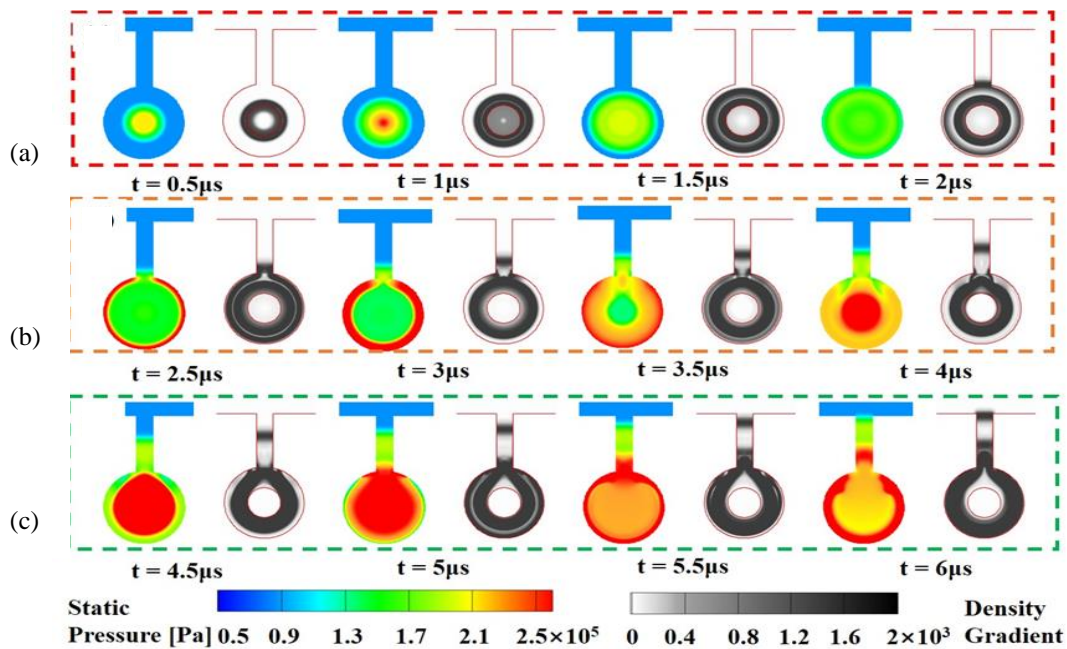

Fig. 9 The internal static pressure and numerical schlieren contour map on the symmetry plane of the normal slot actuator (in the circumferential direction)

the precursor shock waves and jet morphology, along with a notably larger uniform zone. Hence, the experimental findings suggested that the normal slot actuator holds promising potential for flow control applications.

However, due to the limited availability of flow field information in the experiment, the analysis did not provide a detailed explanation for these observed phenomena. This paper aims to elucidate the formation mechanism of the flow field in the normal slot actuator comprehensively, focusing on the evolution of flow field parameters from simulation results and a quantitative assessment of the parameters.

3.1 Analysis of the Internal Flow Field Characteristics of Plasma Synthetic Jet Actuators

To better understand the formation process of the plasma jets and shock waves within the cavity, simulation results are used to depict the evolution of the pressure and numerical schlieren in the flow field of the normal orifice and normal slot actuators. The simulations reveal significant differences in the evolution of the flow fields along the length and circumferential directions of the cavities. A comparative analysis is now conducted of the internal flow field evolution of the normal orifice and normal slot actuators from two perspectives.

Figure 9 illustrates the evolution of the pressure and numerical schlieren in the circumferential direction on the symmetry plane for the normal slot actuator. At 0.5 μs, rapid heating due to arc discharge results in an increased gas temperature and pressure. A distinct pressure jump surface forms between the heated and unheated regions, giving rise to the first precursor shock wave. Simultaneously, the pressure in the arc-heated region, due to continuous heating, significantly exceeds the post-

(a) t = 0.5μs   t = 1μs   t = 1.5μs   t = 2μs

(b) t = 2.5μs   t = 3μs   t = 3.5μs   t = 4μs

(c) t = 4.5μs   t = 5μs   t = 5.5μs   t = 6μs

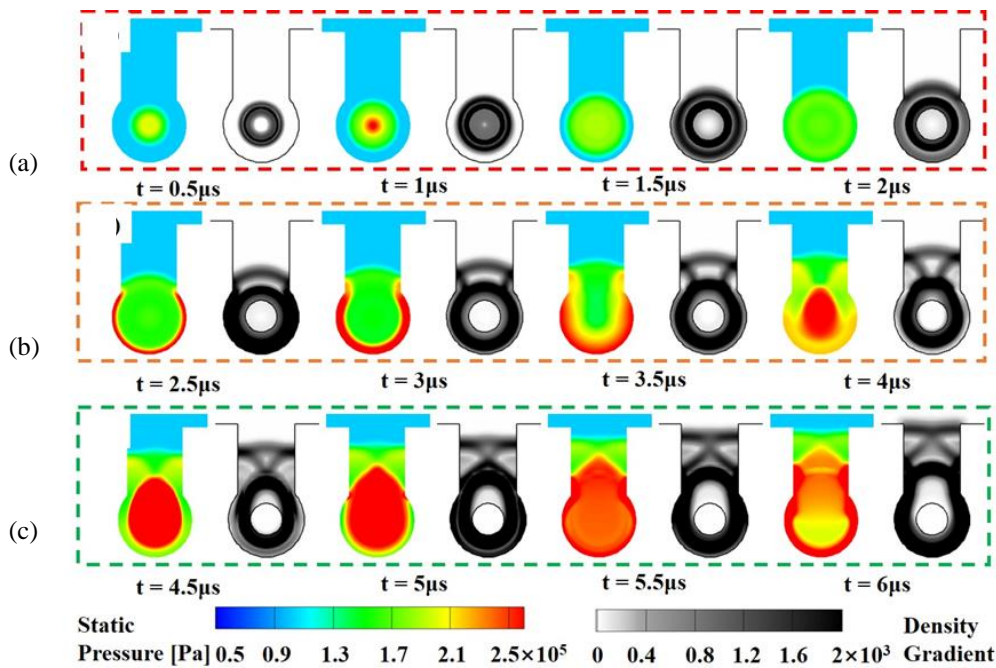Static Pressure [Pa] 0.5 0.9 1.3 1.7 2.1 2.5×10⁵   0 0.4 0.8 1.2 1.6 2×10³ Density Gradient

Fig. 10 The internal static pressure and numerical schlieren contour map on the symmetry plane of the normal orifice actuator (in the circumferential direction)

shock pressure of the first precursor shock wave, creating a second pressure jump surface. The density gradient at 0.5 μs shows a noticeable pressure gradient before and after the first shock wave.

At 2 μs, the first precursor shock wave reaches the cavity wall, initiating the reflection of the shock wave. At 2.5 μs, the compression of the shock wave near the wall results in extremely high pressure. Some waves at the slot exit begin to propagate along the normal slot. Simultaneously, internal waves in the cavity reflect at the wall, and the high-pressure region gradually expands toward the center. At 4 μs, the shock wave reflects back to the arc region, creating another high-pressure region at the center. At this moment, the high-pressure region exhibits a distinct droplet shape, mainly because shock waves at the normal slot do not contribute to its formation. The density gradient also shows that the first precursor shock wave continues to propagate forward along the normal slot. At the slot inlet, intersecting waves are formed as the reflected waves on both sides of the normal slot converge.

At 4.5 μs, the central high-pressure region begins to expand toward the wall. The droplet-shaped high-pressure region becomes more pronounced, reaching the normal slot inlet first, and the second shock wave begins to propagate outward along the normal slot at 5.5 μs. The shock wave reaches the wall again at 5.5 μs, initiating the second reflection process. At 6 μs, the precursor shock wave reaches the normal slot exit. The external flow field characteristics of the jet and moving waves will be analyzed in subsequent sections.

It is noteworthy that during 0–6 μs, shock waves and high-temperature fluid develop within the cavity, demonstrating a strong regularity. The evolution of the flow field within the cavity can be divided into three stages. Figure 9(a) depicts the process of the first shock

wave generation and its movement to the actuator wall. Figure 9(b) illustrates the first reflection process of the shock wave at the wall, forming the first reflected shock wave. Figure 9(c) depicts the second reflection process of the shock wave as the precursor shock wave reaches the slot exit.

Figure 10 illustrates the evolution of the internal flow field of the normal orifice actuator on the circumferential symmetric plane. It can be observed from the figure that the fundamental characteristics of the flow field evolution between the normal orifice actuator and the normal slot actuator are quite similar. The flow evolution of the normal orifice actuator also consists primarily of three stages. Figure 10(a) depicts the formation and movement process of the first shock wave, while Fig. 10(b) shows the first reflection process of the shock wave. Figure 10(c) illustrates the subsequent movement of the shock wave toward the wall and its reflection process.

Notably, there are distinct differences in the detailed features of the flow field evolution between the normal orifice actuator and the normal slot actuator. The normal orifice has a diameter of 1.8 mm, while the normal slot has a width of 0.5 mm. A higher proportion of shock waves propagate outward through the normal orifice, resulting in a faster pressure drop on the outlet side and leading to a visibly longer vertical extent of the droplet-shaped pressure zone. Additionally, due to the larger diameter of the normal orifice, a greater portion of the reflected shock waves enter the outlet. Compared to the normal slot actuator, the reflected shock waves are more pronounced with higher intensity for the normal orifice actuator. These reflected shock waves contribute to poorer pressure uniformity at the outlet of the normal orifice.

The internal flow field in the longitudinal direction of the cavity for the normal slot actuator (Fig. 11) exhibits
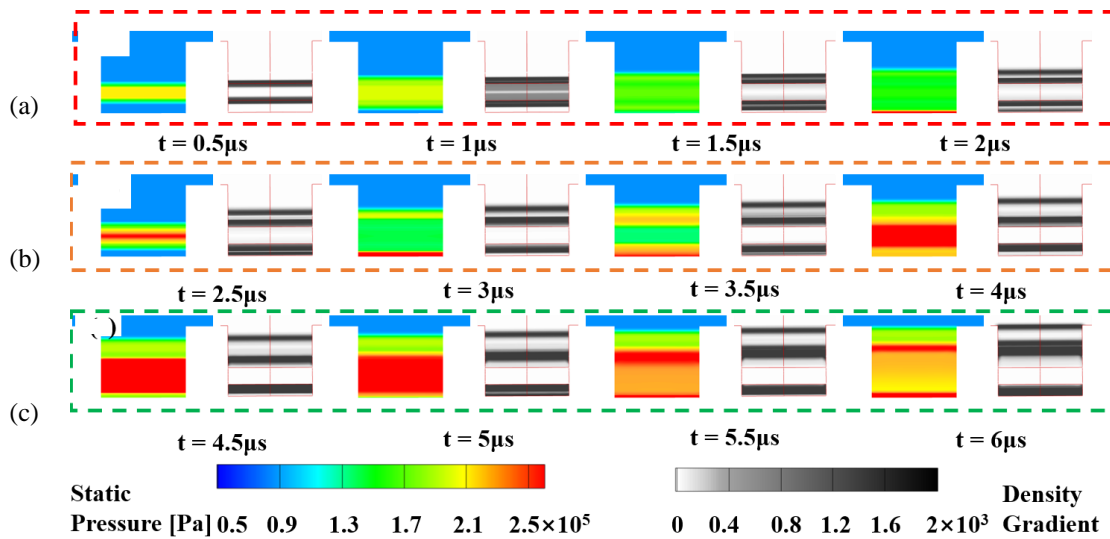
Fig. 11 The internal static pressure and numerical schlieren contour map on the symmetry plane of the normal slot actuator (in the longitudinal direction of the cavity)
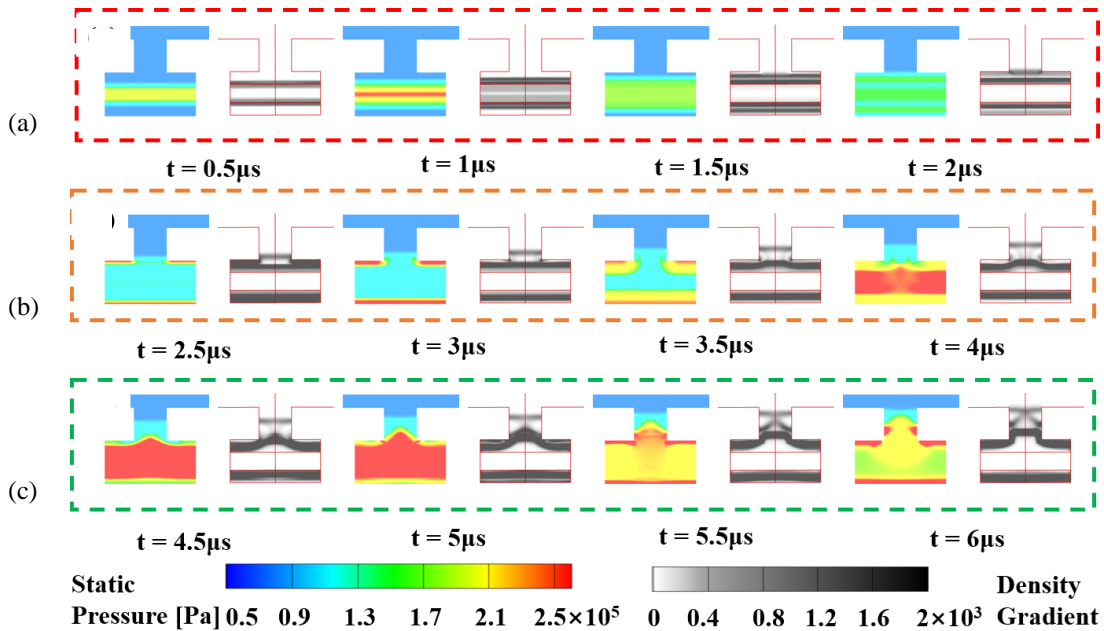

Fig. 12 The internal static pressure and numerical schlieren contour map on the symmetry plane of the normal orifice actuator (in the longitudinal direction of the cavity)

significant differences from that in the circumferential direction. This is primarily attributed to two reasons: 1) distinct geometric constraints along the longitudinal and circumferential directions, and 2) the parallel orientation of the longitudinal direction with the arc, as opposed to the perpendicular alignment of the circumferential direction, leading to significant variations in the flow field. In this direction, multiple instances of shock wave reflections are still observed. The normal slot actuator has a slot length of 5 mm in the longitudinal direction of the cavity, with an electrode spacing of 5 mm. Of particular note is the exceptional uniformity demonstrated by the flow field in this direction. Both the pressure contour map and numerical schlieren image reveal the presence of straight pressure interfaces and straight shock wave fronts. This indicates that the normal slot actuator, when introducing disturbances into the output flow field, provides a region

of significant uniformity in pressure, momentum, and thermal disturbance.

This characteristic is primarily attributed to the parallel formation of the slot outlet and the arc-heating region. The parallel arrangement effectively reduces shock wave reflections, thereby ensuring the uniform characteristics of the flow field. In flow control applications, a uniformly perturbed flow field offers enhanced control capabilities.

The flow field uniformity in the direction of the cavity length perturbation is significantly lower for the normal orifice actuator than for the normal slot actuator. This is primarily attributed to the fact that the jets and shock waves on both sides of the orifice outlet cannot propagate outward through the outlet. Shock waves continuously reflect within the cavity, leading to the formation of reflected shock waves at the outlet. This results in an
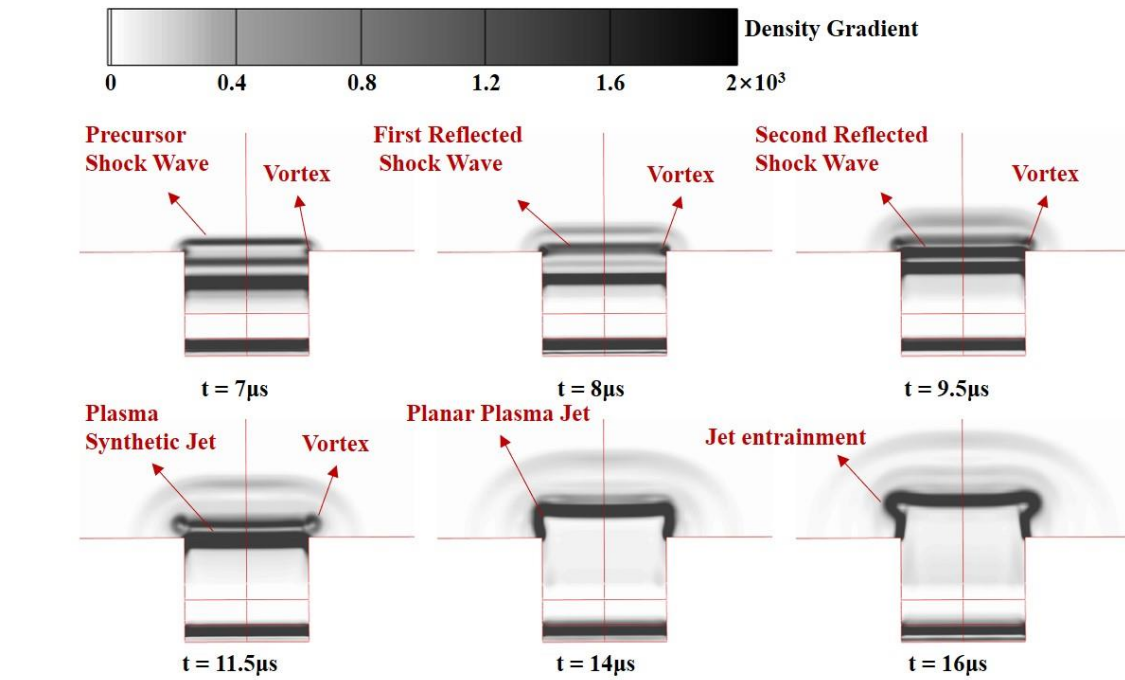
(a) The normal slot actuator.
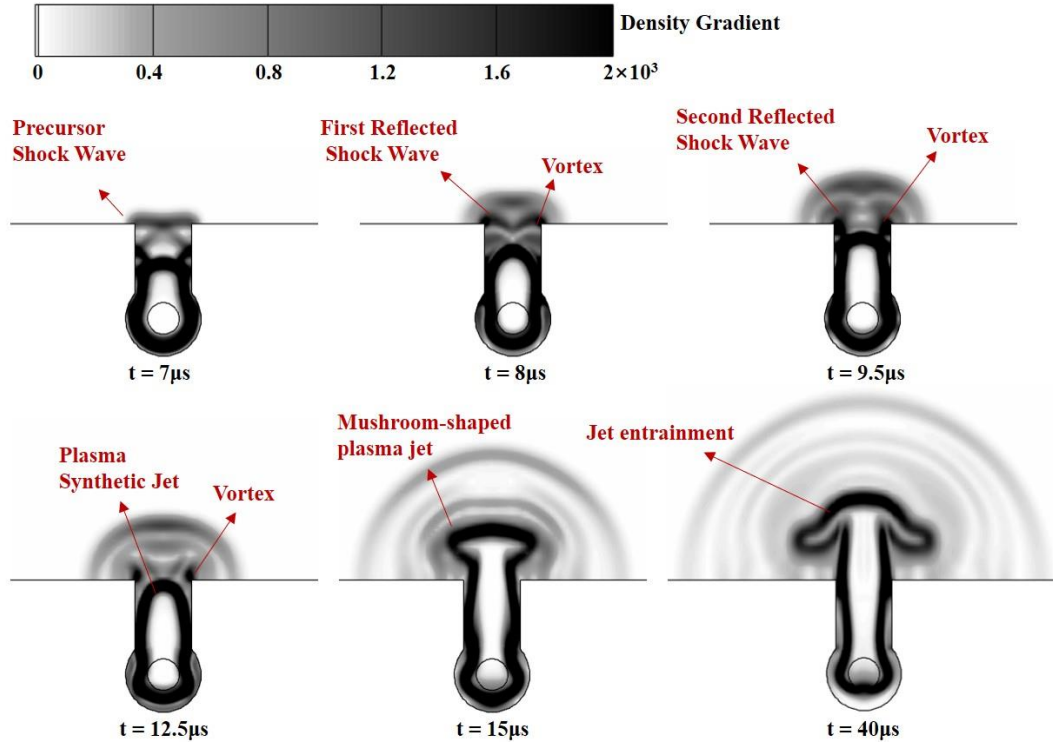
(b) The normal orifice actuator.

Fig. 13 A numerical schlieren contour map of the jet and moving shock wave

uneven pressure distribution, and concurrently, the shape of the shock waves undergoes continuous distortion and deformation. Consequently, the flow field uniformity of the normal orifice actuator is weakened, with the parameters exhibiting considerable spatial variations.

3.2 Jet and Moving Shock Wave Flow Field Characteristics Analysis

In Fig. 13(a), the numerical schlieren evolution of the shockwave from the normal slot actuator reveals the ejection of the precursor shockwave takes place at 7 μs.

The precursor shockwave induces disturbances in the gas, resulting in an increase in the gas pressure behind the wave, causing lateral motion and the subsequent formation of vortices. The first and second reflected shockwaves sequentially exit the outlet at 8 μs and 9.5 μs, respectively, while the vortices gradually enlarge. The characteristic planar shockwave formation of the actuator is noteworthy, as evidenced by a prolonged straight section, primarily attributed to the uniformly distributed and linearly varying pressure behind the precursor shockwave. At 11.5 μs, the plasma synthetic jet begins to

emanate from the outlet, manifesting as a deep black region in the numerical schlieren image. This plasma synthetic jet shows typical high-temperature characteristics with lower density and a significant density gradient to the surrounding gas, resulting in a distinct boundary. Additionally, due to the slot outlet's aspect ratio of 10, the synthetic jet generated by the normal slot actuator also exhibits prominent planar characteristics. Subsequently, the jet undergoes vortex entrainment, with the lower end narrowing and the upper edge widening, and rapid momentum exchange with the external ambient gas.

Similarly, the precursor shockwave from the normal orifice actuator also exits the outlet at 7 μs [Fig. 13(b)]. Simultaneously, two intersecting reflected shockwaves follow the precursor shockwave. Subsequently, the first and second reflected shockwaves exit the outlet sequentially, accompanied by the generation of vortices. However, the exit of the reflected shockwaves is not a unified event; instead, it comprises two intersecting shockwaves collectively propagating outward. From the illustration, it is evident that the shockwaves from the normal orifice actuator exhibit a pronounced spherical shape, indicating weaker uniformity. Furthermore, the jet displays a typical mushroom-shaped profile, with a fast core velocity and slower edge velocities, underscoring the relatively weaker uniformity of the normal slot jet.

3.3 Plasma Synthetic Jet Outlet Flow Field Characteristics Analysis

The outlet parameters of the plasma synthetic jet directly impact its jet control capability. In order to quantitatively compare and analyze the flow field characteristics at the outlets of the normal orifice and normal slot actuators, various flow field parameters were obtained. From the static pressure contour map at the outlet cross-section (Fig. 14), it can be observed that the outlet pressures of both actuators vary over time. This is primarily due to the increasing total pressure within the cavity as heating continues. Simultaneously, due to reflections on the cavity walls, along with the passage of precursor shock waves and reflected shock waves through the outlet cross-section, the pressure also undergoes changes.

The pressure distribution on the outlet cross-section of the normal slot actuator is extremely uniform in space, providing stable and uniform pressure perturbations that contribute to enhancing the flow control capabilities. In contrast, the pressure distribution on the outlet cross-section of the normal orifice actuator is less uniform spatially. This is mainly attributed to the continuous reflection of shock waves on the cylindrical surface and electrode surface. The reflected shock waves lead to an uneven pressure distribution on the outlet cross-section. Because the distances traveled by the shock waves to reach the cylindrical surface and electrode surface differ, the pressure distribution on the circular orifice cross-section sometimes exhibits left-right asymmetry and at other times exhibits top-bottom asymmetry.

The average velocity of the actuator in the outlet section can be used to effectively assess the actuator's momentum input capability. Figure 15(a) shows the
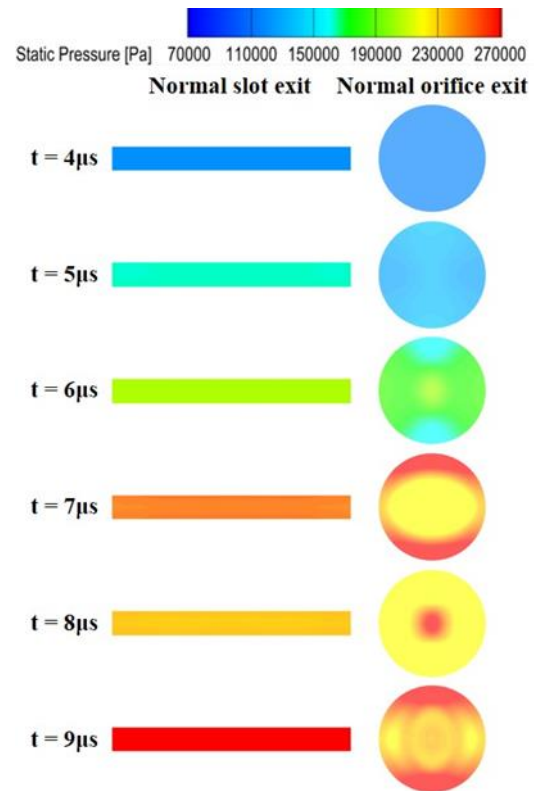

Fig. 14 A comparison of the static pressures at the outlet cross-section

average Mach numbers (Ma) at the exit section, where the Mach number is defined as the ratio of the average exit velocity to the local ambient speed of sound. The normal slot actuator reaches its maximum Mach number of 1.11 at 15 μs, while the normal orifice actuator achieves its maximum Mach number of 1.09 at 17 μs. The normal slot actuator has a higher Mach number peak, indicating better momentum input capability. Additionally, it reaches the peak Mach number in less time, demonstrating a faster momentum output response. In the later stages, the normal slot actuator exhibits slower Mach number decay compared to the normal orifice actuator. From the descent curves, it is evident that the initial slope of the Mach number decay for the normal slot actuator is smaller than that of the normal orifice actuator. However, the velocity decay slopes become comparable thereafter. At 19 μs, the Mach number of the normal slot actuator ceases to decline, entering a plateau phase and maintaining a relatively stable value. This suggests that, compared to the normal orifice actuator, the normal slot actuator has stronger momentum input capability.

To assess the total energy of the jet injection, Fig. 15(b) illustrates the curve of the total pressure ratio, defined as the ratio of the average total pressure of the actuator exit to the ambient total pressure. The average total pressure ratios of the outlet sections of both actuators shows a distinct cyclic oscillation trend, primarily caused by the reflection of shock waves through the jet outlet. The first three half-cycles of oscillation are approximately 1 μs each, with the period mainly related to the geometric dimensions of the actuator. Subsequently, the oscillation period gradually increases, mainly due to the weakening
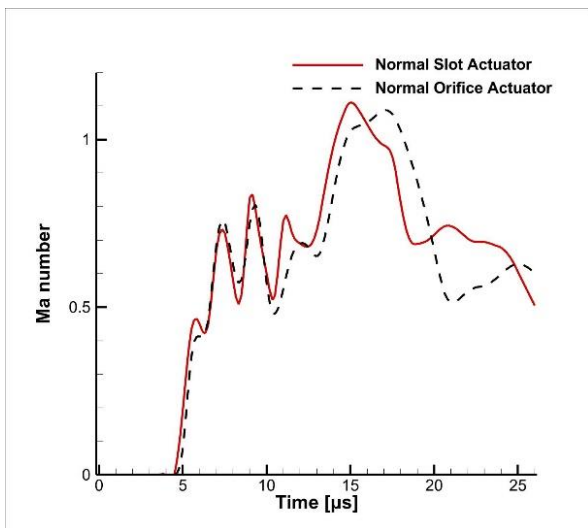
(a) The section average Ma
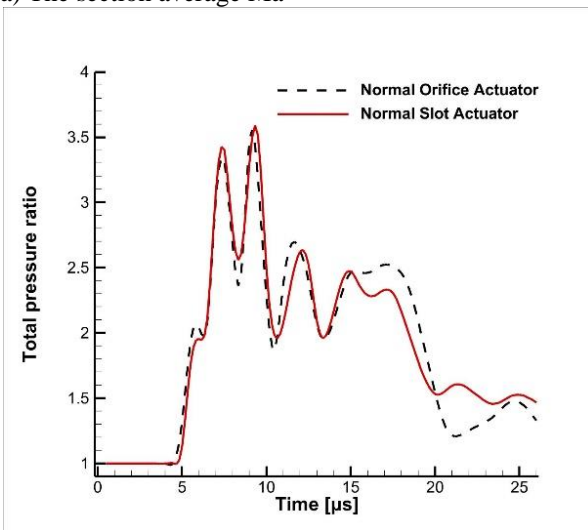
(b) The section average total pressure ratio

Fig. 15. The evolution of the outlet section parameters

of the shock wave intensity and reduced motion velocity after multiple reflections.

The total pressure ratio for the normal slot actuator is 3.59, significantly higher than the 3.50 observed for the normal orifice actuator. Both actuators have the same injection energy. This indicates that the pressure loss caused by the slotted actuator is significantly lower than that caused by the pinhole actuator. The reflection of shock waves is more pronounced in the pinhole actuator, resulting in a more disorderly flow and greater pressure loss.

4. CONCLUSION

Three-dimensional simulation models for both normal slot and normal orifice actuators have been established in this work, followed by a comprehensive comparative analysis of the three-dimensional flow field characteristics associated with the two actuators. The normal slot actuator shows better potential than the normal orifice actuator for flow control. The primary conclusions are as follows:

A comparative analysis of the evolution of the flow field parameters within the cavity revealed that the heating effect of the arc causes a rapid increase in the gas pressure, leading to the generation of precursor shockwaves. A portion of these shockwaves propagate outward through the exit, while the remaining part undergoes multiple reflections within the cavity. It is noteworthy that shockwaves generated in the heating region of the normal slot actuator are parallel to the exit, resulting in a relatively uniform pressure distribution.

At 7.5 µs, the precursor shockwave reaches the exit of the normal slot actuator. Subsequently, reflected shockwaves and high-temperature plasma jets sequentially appear at the exit. Due to an aspect ratio of 10 and a uniform pressure distribution, the moving shockwaves and jets produced by the normal slot actuator exhibit a larger and more uniform region, contributing to enhanced flow control capabilities.

The shockwave pattern of the normal orifice actuator is more complex, with intersecting shockwaves appearing due to reflections. Additionally, the shockwaves exhibit typical spherical wave characteristics with weaker uniformity. Moreover, due to the shearing effect at the circular orifice exit, the jet morphology manifests as a typical mushroom shape, with a fast core region and lower velocities on the sides. The uneven distribution of the shockwaves and jets complicates the application of the actuator.

The normal slot actuator reaches its maximum Mach number of 1.11 at 15 µs, while the normal orifice actuator achieves its maximum Mach number of 1.09 at 17 µs. The normal slot actuator attains a greater peak Mach number, indicating superior momentum input capability. In addition, it achieves the peak Mach number in a shorter time, demonstrating a faster momentum output response.

The total pressure ratio for the normal slot actuator is 3.59, significantly higher than the value of 3.50 observed for the normal orifice actuator. This indicates that the pressure loss induced by the normal slot actuator is significantly lower than that of the round-hole actuator.

CONFLICT OF INTEREST

The authors declare that they have no known competing financial interests or personal relationships that could have appeared to influence the work reported in this paper.

AUTHORS CONTRIBUTION

Lin Cheng: Conceptualization, Methodology, Investigation, Writing Original Draft. **X. L. Sun**: Software, Formal Analysis, Visualization, Writing - Original Draft. **S. Ma**: Validation, Resources, Writing - Review & Editing, Supervision.

All authors have read and approved the final version of the manuscript.

REFERENCES

Abdollahzadeh, M., Pascoa, J. C., & Oliveira, P. J. (2018). Comparison of DBD plasma actuators flow control authority in different modes of actuation. *Aerospace Science and Technology, 78*, 183–196. https://doi.org/10.1016/j.ast.2018.04.013

Ansys® Fluent, Release 2020 R2

Ansys® ICEM CFD, Release 2020 R2

Bayindirli, C. (2019). Drag reduction of a bus model by passive flow canal. *International Journal of Energy Applications and Technologies, 6*(1), 24–30. https://doi.org/10.31593/ijeat.533745

Bayindirli, C. (2023). Numerical and experimental enhancement of the aerodynamic performance of a road vehicle using passive flow control. *Journal of Applied Fluid Mechanics, 16,* 1414-1426. https://doi.org/10.47176/jafm.16.07.1760.

Bayindirli, C., & Celik, M. (2023). Experimental optimization of aerodynamic drag coefficient of a minibus model with non-smooth surface plate application. *Journal of Engineering Studies and Research, 28*(4), 34–40. https://doi.org/10.29081/jesr.v28i4.004

Belinger, A., Hardy, P., Barricau, P., Cambronne, J. P., & Caruana, D. (2011). Influence of the energy dissipation rate in the discharge of a Plasma Synthetic Jet Actuator. *Journal of Physics D: Applied Physics, 44*(36), 365201. https://doi.org/10.1088/0022-3727/44/36/365201

Cattafesta, L. N. (2017). *Active flow control-introduction.* VKI Lecture Series. https://doi.org/10.35294/ls201704.cattafesta1

Cheng, L., Sun, S., Tan, H. J., Zhang, Y. C. & He, X. M. (2017). Experimental study on characteristics of plasma synthetic actuator with normal slot. *Journal of Propulsion Technology*, (38), 1937-1942. (in Chinese). https://link.cnki.net/doi/10.13675/j.cnki.tjjs.2017.09.003

Cybyk, B., Grossman, K., & Wilkerson, J. (2004). *Performance characteristics of the SparkJet flow control actuator*. 2nd AIAA Flow Control Conference. https://doi.org/10.2514/6.2004-2131

Cybyk, B., Grossman, K., Wilkerson, J., Chen, J., & Katz, J. (2005). *Single-pulse performance of the sparkjet flow control actuator*. 43rd AIAA Aerospace Sciences Meeting and Exhibit. https://doi.org/10.2514/6.2005-401

Cybyk, B., Land, H., Simon, D., Chen, J., & Katz, J. (2006). *Experimental characterization of a supersonic flow control actuator*. 44th AIAA Aerospace Sciences Meeting and Exhibit. https://doi.org/10.2514/6.2006-478

Ebrahimi, A., & Hajipour, M. (2018). Flow separation control over an airfoil using dual excitation of DBD plasma actuators. *Aerospace Science and Technology, 79*, 658–668. https://doi.org/10.1016/j.ast.2018.06.019

Ebrahimi, A., Hajipour, M., & Ghamkhar, K. (2018). Experimental study of stall control over an airfoil with dual excitation of separated shear layers. *Aerospace Science and Technology, 82–83*, 402–411. https://doi.org/10.1016/j.ast.2018.09.027

Emerick, T., Ali, M. Y., Foster, C., Alvi, F. S., & Popkin, S. (2014). SparkJet characterizations in quiescent and supersonic flowfields. *Experiments in Fluids, 55*(12). https://doi.org/10.1007/s00348-014-1858-6

Falempin, F., Фирсов, A. A., Yarantsev, D., Goldfeld, M. A., Timofeev, K., & Leonov, S. B. (2015). Plasma control of shock wave configuration in off-design mode of M = 2 inlet. *Experiments in Fluids, 56*(3), https://doi.org/10.1007/s00348-015-1928-4

Grossman, K., Bohdan, C., & VanWie, D. (2003). *Sparkjet actuators for flow control.* 41st Aerospace Sciences Meeting and Exhibit. https://doi.org/10.2514/6.2003-57

Haack, S., Taylor, T., Cybyk, B., Foster, C., & Alvi, F. (2011). *Experimental estimation of SparkJet efficiency.* 42nd AIAA Plasmadynamics and Lasers Conference. https://doi.org/10.2514/6.2011-3997

Haack, S., Taylor, T., Emhoff, J., & Cybyk, B. (2010). *Development of an analytical SparkJet model.* 5th Flow Control Conference. https://doi.org/10.2514/6.2010-4979

Kim, H. J., Shin, J. Y., Ahn, S., & Kim, K. H. (2019). *Numerical analysis on flow characteristics and jet boundary condition of Sparkjet actuator*. AIAA Scitech 2019 Forum. https://doi.org/10.2514/6.2019-0736

Lapushkina, T. A., Erofeev, A. V., Azarova, O. A., & Kravchenko, O. V. (2019). Interaction of a plane shock wave with an area of ionization instability of discharge plasma in air. *Aerospace Science and Technology, 85*, 347–358. https://doi.org/10.1016/j.ast.2018.12.020

Liu, F., Yan, H., Zhan, W., & Xue, Y. (2019). Effects of steady and pulsed discharge arcs on shock wave control in mach 2.5 flow. *Aerospace Science and Technology, 93*, 105330. https://doi.org/10.1016/j.ast.2019.105330

Luo, Y., Li, J., Liang, H., Guo, S., Tang, M., & Wang, H. (2021). Suppressing unsteady motion of shock wave by high-frequency plasma synthetic jet. *Chinese*

Journal of Aeronautics, 34(9), 60–71. https://doi.org/10.1016/j.cja.2021.04.011

Meng, X., Hu, H., Yan, X., Liu, F., & Luo, S. (2018). Lift improvements using duty-cycled plasma actuation at low Reynolds numbers. *Aerospace Science and Technology, 72*, 123–133. https://doi.org/10.1016/j.ast.2017.10.038

Miao, H., Zhang, Z., Wu, Y., He, Y., & li, Y. (2021). A self-trigger three-electrode plasma synthetic jet actuator. *Sensors and Actuators A: Physical, 332*, 113174. https://doi.org/10.1016/j.sna.2021.113174

Narayanaswamy, V., Raja, L. L., & Clemens, N. T. (2010). Characterization of a high-frequency pulsed-plasma jet actuator for supersonic flow control. *AIAA Journal, 48*(2), 297–305. https://doi.org/10.2514/1.41352

Shaygani, A., & Adamiak, K. (2023). Mean model of the dielectric barrier discharge plasma actuator including photoionization. *Journal of Physics D: Applied Physics, 56*(5), 055203. https://doi.org/10.1088/1361-6463/acaa43

Wang, L., Luo, Z. B., Xia, Z. X., & Liu, B. (2013). Energy efficiency and performance characteristics of plasma synthetic jet. *Acta Physica Sinica, 62*(12), 125207. https://doi.org/10.7498/aps.62.125207

Zhang, W., Geng, X., Shi, Z., & Jin, S. (2020). Study on inner characteristics of plasma synthetic jet actuator and geometric effects. *Aerospace Science and Technology, 105*, 106044. https://doi.org/10.1016/j.ast.2020.106044

Zhang, W., Shi, Z., Li, Z., Geng, X., Zhang, C., & Sun, Q. (2022a). Study on propagation mechanisms of the actuations generated by plasma synthetic jet actuator in a supersonic flow. *Aerospace Science and Technology, 126*, 107644. https://doi.org/10.1016/j.ast.2022.107644

Zhang, W., Shi, Z., Zhang, C., Geng, X., Li, K., & Chen, Z. (2022b). A study on flow control in a hypersonic inlet using a plasma synthetic jet actuator. *Physics of Fluids, 34*(10). https://doi.org/10.1063/5.0114073

Zhang, X., Zhao, Y., & Yang, C. (2023). Recent developments in thermal characteristics of surface dielectric barrier discharge plasma actuators driven by sinusoidal high-voltage power. *Chinese Journal of Aeronautics, 36*(1), 1–21. https://doi.org/10.1016/j.cja.2022.01.026

Zheng, B., Zhang, Q., Zhao, T., Song, G., & Chen, Q. (2023). Experimental and numerical investigation of a self-supplementing dual-cavity plasma synthetic jet actuator. *Plasma Science & Technology, 25*(2), 025503. https://doi.org/10.1088/2058-6272/ac8cd4

Zong, H., & Kotsonis, M. (2019). Effect of velocity ratio on the interaction between plasma synthetic jets and turbulent cross-flow. *Journal of Fluid Mechanics, 865*, 928–962. https://doi.org/10.1017/jfm.2019.93

Zong, H., Chiatto, M., Kotsonis, M., & de Luca, L. (2018). Plasma synthetic jet actuators for active flow control. *Actuators, 7*(4), 77. https://doi.org/10.3390/act7040077